Research Square

Preprints are preliminary reports that have not undergone peer review.
They should not be considered conclusive, used to inform clinical practice,
or referenced by the media as validated information.

Probabilistic assessment of windblown sand hazard across a desert photovoltaic site using terrain-downscaled reanalysis winds

Sai Li

sjzlisai@foxmail.com

Shijiazhuang Tiedao University https://orcid.org/0000-0002-2920-8556

Wenyong Ma

Shijiazhuang Tiedao University

Bingbing Wang

CHN Energy New Energy Technology Research Institute Co., Ltd.

Lingui Xin

CHN Energy New Energy Technology Research Institute Co., Ltd.

Junxiang Ma

East China Electric Power Design Institute Co., Ltd. of China Power Engineering Consulting Group

Research Article

Keywords: Desert photovoltaic site, Aeolian sand transport, Flux potential, Terrain wind downscaling, Monte Carlo simulation

Posted Date: November 3rd, 2026

DOI: https://doi.org/10.21203/rs.3.rs-10918084/v1

License: This work is licensed under a Creative Commons Attribution 4.0 International License.
Read Full License

Probabilistic assessment of windblown sand hazard across a desert photovoltaic site using terrain-downscaled reanalysis winds

Sai Li[a,b], Wenyong Ma[a,b,c*], Bingbing Wang[d], Lingui Xin[d], Junxiang Ma[e]

[a] Key Laboratory of Roads and Railway Engineering Safety Control (Shijiazhuang Tiedao University), Ministry of Education, Shijiazhuang 050043, China

[b] School of Civil Engineering, Shijiazhuang Tiedao University, Shijiazhuang 050043, China

[c] Innovation Center for Wind Engineering and Wind Energy Technology of Hebei Province, Shijiazhuang 050043, China

[d] CHN Energy New Energy Technology Research Institute Co., Ltd., Beijing 102209, China

e East China Electric Power Design Institute Co., Ltd. of China Power Engineering Consulting Group, Shanghai 200063, China

* Corresponding author: Wenyong Ma

Address: No. 17, North Second Ring Road East, Shijiazhuang City, Hebei Province, China 050043

E-mail: ma@stdu.edu.cn

Probabilistic assessment of windblown sand hazard across a desert photovoltaic site using terrain-downscaled reanalysis winds

Abstract: Windblown sand hazard at desert photovoltaic (PV) sites is commonly assessed using coarse regional winds or local array scale experiments, leaving dune scale spatial variability poorly resolved. An hourly probabilistic framework was developed to resolve spatial variations in sand-drift potential. Dune morphology was derived from a digital elevation model, and hourly ERA5 winds for 2021–2023 were downscaled to 30 m using a conservation of mass solver. The downscaling method was independently validated and showed good agreement with field observations ($r = 0.949$). The downscaled winds were converted into hourly potential sand transport and aggregated into flux potential (FP) and other transport indicators. Uncertainty in threshold friction velocity and representative annual winds was propagated to PV subarray estimates through Monte Carlo simulation. Terrain downscaling produced acceleration over crests and upper slopes and deceleration in interdune and sheltered terrain. Dunes in more exposed surroundings exhibited higher overall FP, while local hotspots clustered near crests and upper windward slopes, where FP reached approximately three times the dune mean. High transport crest zones generally showed greater directional variability than lower leeward areas. Monte Carlo analysis broadened annual FP distributions without obscuring terrain-controlled spatial contrasts. The five activity classes remained clearly separated, with median FP decreasing from 71.88 $m^3\ m^{-1}\ yr^{-1}$ in Class I to 60.40 $m^3\ m^{-1}\ yr^{-1}$ in Class V, while the 5th percentile of Class I exceeded the 95th percentile of Class V. The framework supports targeted sand control planning in desert PV development.

Keywords: Desert photovoltaic site; Aeolian sand transport; Flux potential; Terrain wind downscaling; Monte Carlo simulation.

1 Introduction

Utility-scale solar photovoltaic (PV) development has expanded rapidly, including in desert regions where strong solar resources and comparatively low land costs favor large projects (Kruitwagen et al. 2021; Lu et al. 2021). These projects are situated at the interface between aeolian processes and exposed infrastructure. Wind erosion, drifting sand, and sand encroachment can create persistent operational and maintenance hazards (Al-Hemoud et al. 2026; Bruno et al. 2018). Their mitigation depends on identifying where hazardous processes are concentrated within project boundaries. Desert PV hazard assessment must therefore resolve the spatial variability of windblown sand intensity across dunes and infrastructure units.

Assessing sand-drift hazard within desert PV sites requires estimates of both magnitude and directionality. Sand flux driven by effective shear velocity reflects the transport capacity of the wind field and provides a physical basis for evaluating aeolian activity (Kok et al. 2012; Tadesse et al. 2022). The drift potential framework of Fryberger and Dean (1979) allows transport potential and resultant direction to be compared across wind regimes. In this framework, flux potential (FP) represents total potential sand flux integrated over all transport directions, whereas resultant flux potential (RFP) represents net transport potential in the resultant direction. These indicators have been used to quantify aeolian activity and sand-transport potential in dune fields and dryland environments (Gunn et al. 2022). However, most sand-flux assessments still rely on point-scale meteorological observations (Yizhaq et al.

2020) or coarse-resolution reanalysis products (Muñoz-Sabater et al. 2021), which cannot resolve where sand-drift hazard is concentrated across a desert PV site.

An intermediate-scale gap remains between regional hazard characterization and array-scale process studies. Li et al. (2024), for example, quantified mean sand flux across global desert regions using hourly ERA5-Land winds, whereas Tang et al. (2021) examined near-surface aeolian transport and erosion-deposition patterns around PV arrays. Preventive management, however, is implemented within already selected project boundaries, where dune morphology and slope position redistribute regional wind forcing. Digital elevation models (DEMs) can characterize dune morphological features (Hugenholtz et al. 2012). Airflow over dunes generates distinct acceleration and deceleration patterns across windward slopes, crests, and lee slopes (Wiggs et al. 1996). Resolving this within-site variability is necessary to translate regional aeolian conditions into hazard zoning, spatial planning, and targeted remedial measures for desert PV infrastructure.

A practical route to resolving site-scale aeolian variability is to combine hourly reanalysis data with terrain-aware wind downscaling. Reanalysis products provide spatially continuous background conditions, but their coarse resolution cannot represent dune relief, while short-duration strong winds may contribute disproportionately to sand transport (Ren et al. 2024). Available approaches include the Weather Research and Forecasting (WRF) model, conservation-of-mass and momentum (CMM) models, computational fluid dynamics (CFD) models, and conservation-of-mass (COM) models. WRF captures mesoscale circulation and boundary-layer processes but is less efficient for DEM-scale correction within individual PV sites (Powers et al. 2017). CMM and CFD models resolve separation and wakes in greater detail, although they require case-specific boundary conditions and high computational costs (Wagenbrenner et al. 2019). By contrast, COM models efficiently redistribute background winds over complex terrain while preserving mass continuity (Liston and Elder 2006; Forthofer et al. 2014). Their modest input requirements and computational efficiency make them suitable for long-term hourly site-scale assessment, despite their limited representation of detailed flow physics (Wagenbrenner et al. 2016).

Threshold friction velocity, which governs sand entrainment, is another source of uncertainty. Drift-potential and sand-flux calculations commonly use a single threshold determined primarily by grain size (Kok et al. 2012). This assumption allows spatial comparisons under consistent conditions, but the selected value strongly affects estimated transport magnitude. In natural sand beds, threshold conditions also vary with bed microstructure, surface state, and measurement method (Raffaele et al. 2016). This variability may propagate to FP and RFP when combined with hourly wind fluctuations and the nonlinear response of sand transport (Gageik et al. 2024). A probabilistic treatment is therefore needed to separate consistent spatial patterns from uncertainty in absolute transport magnitude.

To connect regional wind forcing with site-scale terrain effects and account for uncertainty in sand entrainment, this study develops a probabilistic dune-scale framework for assessing sand-drift potential within a desert PV site in the Ulan Buh Desert. Dune morphology is characterized using a 30 m digital elevation model, and hourly ERA5 winds from 2021 to 2023 are downscaled using the COM solver. The terrain-induced wind speed variations reproduced by the solver are first evaluated against measurements from the Askervein Hill field experiment. The downscaled hourly wind fields are then used to calculate potential sand transport and aggregate flux potential and resultant flux potential at the site, dune, and PV-subarray scales. Uncertainty in threshold friction velocity and wind conditions is

incorporated through a Monte Carlo procedure. The resulting framework characterizes the spatial differentiation and uncertainty of potential aeolian activity, providing a basis for risk zoning, protection prioritization, and layout optimization within desert PV sites.

2 Study area and data

The study area is a desert PV project site in the hinterland of the Ulan Buh Desert, northern China. The center of the project area is located at 106.330°E, 39.715°N (Fig. 1). Terrain information was derived from the Copernicus GLO-30 digital elevation model (European Space Agency 2024). The site lies within an undulating dune landscape with elevations of approximately 1090-1250 m. The northwestern part of the study area is relatively open and low-relief, whereas higher and more continuous dune relief occurs toward the southeast.

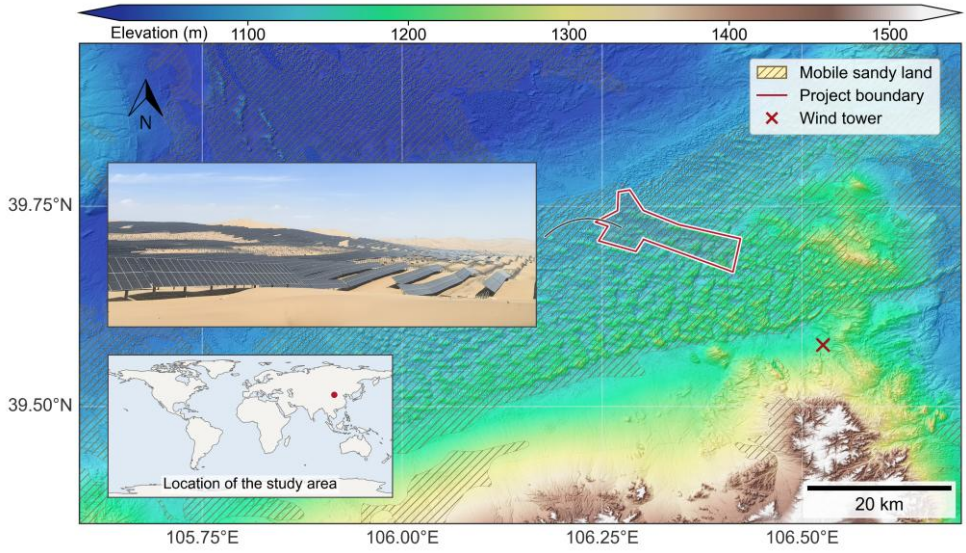


Fig. 1 Study-area setting in the Ulan Buh Desert: project boundary, topographic elevation, mobile sandy land, auxiliary meteorological mast, and representative field conditions.

The shaded areas in Fig. 1 show the distribution of mobile sandy land, derived from the 1:10^5 Desert Distribution Atlas of China (Wang et al. 2013). Mobile sandy land is widely distributed within and around the project boundary. The surface material is dominated by loose fine sand, with a natural unit weight of 15.0 kN m^{-3}, an internal friction angle of 15.6°, and a median grain size of 0.21 mm. Together with sparse vegetation and dense dune relief, these surface conditions indicate high sensitivity to wind erosion, sand burial, and dust transport under strong wind conditions.

Wind observations were obtained from an auxiliary meteorological mast located approximately 23 km southeast of the project center. The mast is at 106.526°E, 39.577°N and 1216 m elevation, outside the core computational domain. 7 anemometer and wind-vane groups recorded conditions at uneven heights between 10 and 150 m from 1 March 2021 to 28 February 2022. After quality control, 7482 hourly records were retained.

ERA5 reanalysis data were used as the long-term meteorological forcing for the aeolian assessment. ERA5 is the fifth-generation global atmospheric reanalysis released by the European Centre for Medium-Range Weather Forecasts and provides spatially continuous hourly near-surface meteorological variables by assimilating multiple

sources of observations (Hersbach et al. 2023). In this study, hourly ERA5 data from 2021 to 2023 were used at 0.25° × 0.25° resolution. The variables include 10 m zonal and meridional wind components, 2 m air temperature, and cloud cover. Wind speed and wind direction were calculated from the two horizontal wind components, whereas air temperature and cloud cover were retained as thermal-condition inputs for terrain downscaling.

An auxiliary consistency check compared ERA5 values interpolated to the mast location using inverse distance weighting with mast observations over the mast year (Fig. S1). Both datasets indicate prevailing winds from the west to southwest, whereas ERA5 shows a smoother directional distribution and generally lower monthly mean wind speeds. These differences arise because ERA5 represents spatially averaged regional conditions, whereas the mast records point-scale winds influenced by local terrain and surface roughness. The overall consistency therefore supports the use of ERA5 as representative regional forcing for the multi-year aeolian assessment.

3 Methods

3.1 Aeolian assessment framework

This study develops a probabilistic framework for assessing sand-drift potential within a desert PV site using terrain downscaled reanalysis winds (Fig. 2). The workflow links regional meteorological forcing, terrain wind downscaling, hourly potential sand-flux calculation, deterministic sand-transport characterization, and stochastic sand-wind probability (SWP) assessment.

ERA5 hourly fields were processed to define the regional forcing, downscaled over the DEM, and converted into hourly potential sand fluxes. These fluxes were then used for deterministic sand-transport characterization and stochastic SWP assessment, as detailed in the following sections.

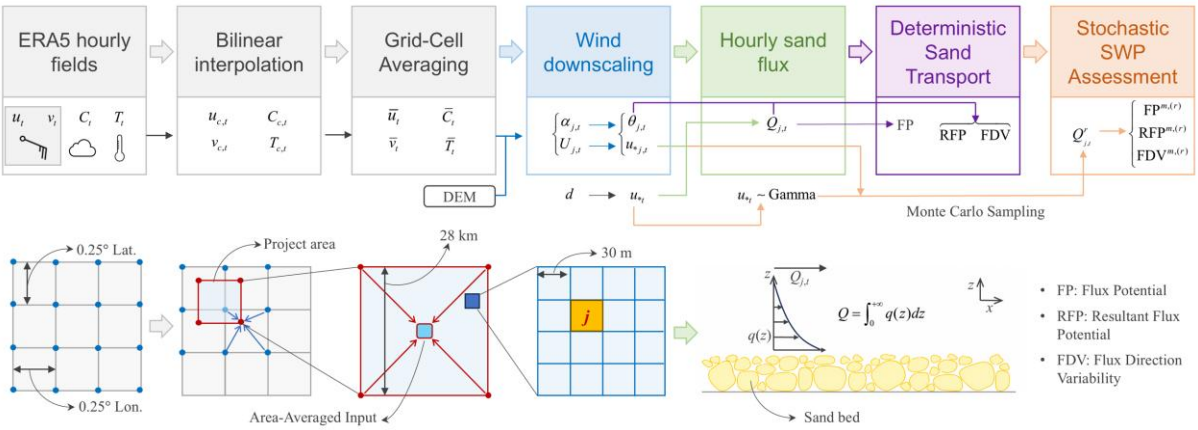


Fig. 2 Integrated workflow for deterministic sand-transport characterization and stochastic sand-wind probability (SWP) assessment within a desert photovoltaic site using terrain-downscaled ERA5 hourly winds.

3.2 Regional mean meteorological input

ERA5 hourly fields provided the external meteorological forcing for the site domain. For each hour t, the variables extracted from ERA5 were the 10 m zonal wind component u_t, the 10 m meridional wind component v_t, the 2 m air temperature T_t, and cloud cover C_t.

Because the ERA5 grid is much coarser than the project domain, each ERA5 variable was first bilinearly interpolated from the surrounding grid cells to the four corners of the computational domain, as shown in Fig. 2. This step produced four corner time series for each hour, denoted as $u_{c,t}$, $v_{c,t}$, $T_{c,t}$, and $C_{c,t}$, where c = 1, 2, 3, and 4 is the corner index. The four corner values were then arithmetically averaged to obtain the domain-mean inputs $\bar{u}_t$, $\bar{v}_t$, $\bar{T}_t$, and $\bar{C}_t$. The averaged wind components $\bar{u}_t$ and $\bar{v}_t$ were further converted to the regional mean 10 m wind speed $\bar{U}_t$ and meteorological wind direction $\bar{\alpha}_t$. Finally, $\bar{U}_t$, $\bar{\alpha}_t$, $\bar{T}_t$, and $\bar{C}_t$ were used as the hourly regional background meteorological inputs for wind downscaling.

3.3 Terrain wind downscaling

Hourly near-surface wind fields were generated by coupling the regional forcing described in Section 3.2 with the project DEM in WindNinja 3.12.2. WindNinja is an open-source diagnostic terrain-wind model that accepts a DEM, surface properties, and an initial wind specified as a domain-averaged initial wind field. Within WindNinja, the COM solver adjusts the initialized three-dimensional wind field to satisfy incompressible mass continuity while minimizing its departure from the background field (Forthofer et al. 2014). Unlike direct interpolation of ERA5 winds, this adjustment redistributes the background flow in response to terrain slope and elevation while retaining the regional forcing (Wagenbrenner et al. 2016).

To formulate the regional input for COM, the hourly domain-mean wind was treated as the initial field $\hat{u}_t$ in an east–north–up coordinate system. The horizontal components were prescribed as $\hat{u}_{1,t} = \bar{u}_t$ and $\hat{u}_{2,t} = \bar{v}_t$, while the vertical component was determined by the terrain boundary condition. For each hour, the adjusted field $u = (u_1, u_2, u_3)$ is obtained by minimizing its weighted departure from the initial field while imposing incompressible continuity, $\nabla \cdot u = 0$. The objective functional is

$$E_t(u_1,u_2,u_3) = \int_\Omega \left[a_1^2 \left(u_1 - \hat{u}_1\right)^2 + a_1^2 \left(u_2 - \hat{u}_2\right)^2 + a_2^2 \left(u_3 - \hat{u}_3\right)^2 \right] d\Omega \qquad (1)$$

where Ω is the computational domain, and a_1 and a_2 are Gaussian precision moduli that weight allowable horizontal and vertical corrections. A Lagrange multiplier converts this constrained minimization into an elliptic equation; solving it under terrain-impermeability and open-boundary conditions provides the velocity correction applied to the initial field. COM therefore produces a mass-consistent wind field through the smallest weighted adjustment of the background flow rather than by solving the full momentum equations.

The diurnal slope-flow and non-neutral atmospheric stability parameterizations were enabled. The domain mean 2 m air temperature and cloud cover passed from Section 3.2 supplied the thermal inputs used by WindNinja to estimate surface radiation and sensible heating, modify near-surface stability, and add first-order diurnally driven slope-flow components (Wagenbrenner et al. 2019). This treatment incorporates terrain and near-surface thermal modulation without invoking the momentum-resolving CFD solver.

For every grid cell j and hour t, the retained outputs were the downscaled 10 m wind speed $U_{j,t}$ and meteorological wind direction $\alpha_{j,t}$ on the approximately 30 m DEM grid. As shown in Fig. 2, these two fields form the direct inputs to Section 3.5, where wind direction is converted to transport-to direction and wind speed to friction velocity before hourly potential transport is calculated. The same configuration was applied to all 26,280 hours from 2021–2023.

3.4 Validation of terrain wind downscaling

Independent validation used field measurements from Askervein Hill, a geometrically simple landform with approximately 108 m relief and a horizontal scale of about 3 km. The combined MF03-D/TU03B dataset provides 10 m wind speeds at 40 comparison instruments distributed along Transects A–C, together with an upstream reference station approximately 3 km from the hill (Fig. 3). During the selected period, the reference station recorded an approach flow of 8.9 m s^{-1} from 210° under near-neutral conditions, with Richardson numbers ranging from −0.0110 to −0.0074 (Taylor and Teunissen 1987).

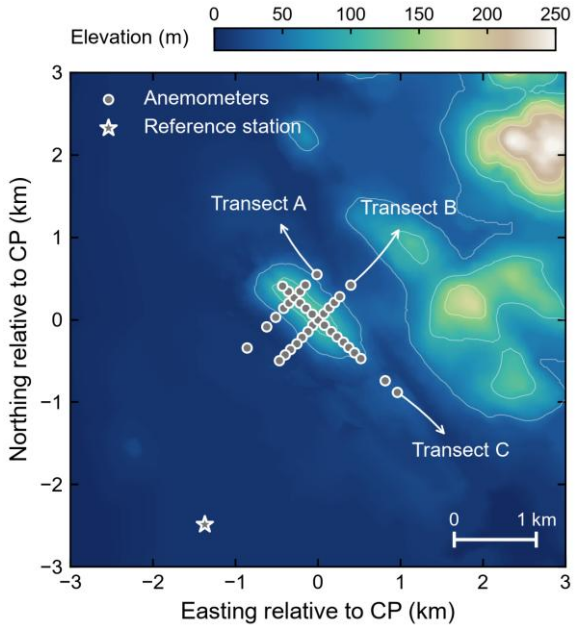


Fig. 3 Askervein Hill elevation and 10 m observation locations used for independent COM validation. Coordinates are relative to the hill centre point (CP).

The Askervein MF03-D/TU03B case was simulated using the WindNinja COM solver over a 6 × 6 km contour-derived terrain domain with an underlying horizontal resolution of approximately 23 m. An upstream reference wind speed of 8.9 m s^{-1} from 210° was prescribed, and the resulting 10 m wind field was exported on a 43 m grid. The modelled wind-speed distribution and terrain-elevation contours are shown in Fig. S2.

For the three selected transects, the along-transect comparisons show that COM captured the observed increase in wind speed toward exposed upper terrain and the subsequent reduction away from the crest (Fig. 4a–c). The largest discrepancy occurred along Transect A, particularly near the foot of the leeward slope, where COM substantially overestimated the observed wind speed and did not fully reproduce the pronounced local deceleration. Agreement was generally better along Transects B and C. Transect-specific correlations were r = 0.888, 0.965, and 0.933 for Transects A, B, and C, respectively.

Across all 40 comparison instruments, the aggregate comparison yielded an RMSE of 1.16 m s^{-1}, an MAE of 0.90 m s^{-1}, and a Pearson correlation coefficient (r) of 0.949 (Fig. 4d). Overall, the model–observation comparison indicates satisfactory agreement for the intended use of COM to represent relative terrain-induced wind-speed redistribution in the multi-year assessment.

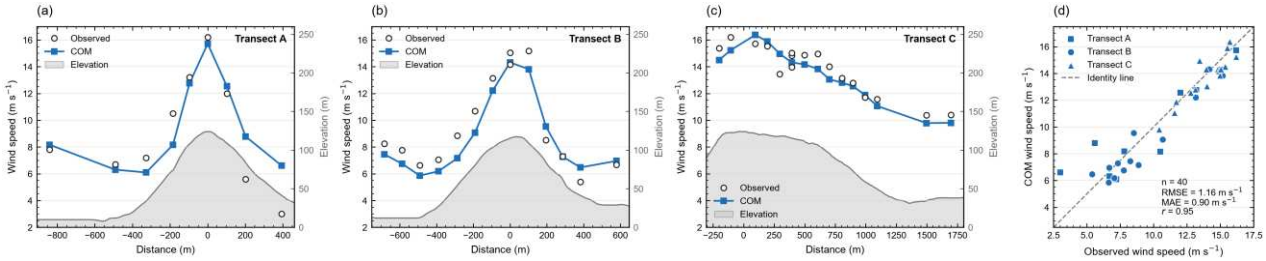


Fig. 4 Independent WindNinja COM validation for Askervein case MF03-D/TU03B. (a–c) Observed and modelled 10 m wind speeds along Transects A–C. (d) Modelled versus observed wind speed for all 40 instruments.

3.5 Hourly potential sand transport calculation

WindNinja reports meteorological wind direction, defined as the direction from which the wind blows, whereas sand moves downwind. The transport-to direction at grid point j and hour t was therefore defined as $\theta_{j,t} = \mathrm{mod}(\alpha_{j,t} + 180°, 360°)$. To convert the downscaled 10 m wind speed into a dynamic variable directly related to sand entrainment, friction velocity was calculated using the neutral logarithmic wind profile,

$$u_{*,j,t} = \frac{\kappa U_{j,t}}{\ln\left(z / z_0\right)} \tag{2}$$

where $u_{*j,t}$ is the friction velocity at grid point j and hour t, $\kappa = 0.41$ is the von Karman constant, $z = 10$ m is the reference height, and $z_0 = 0.004$ m is the aerodynamic roughness length estimated from the on-site mast observations.

The threshold friction velocity u_{*t} is the critical value required for saltation to begin from a static sand bed. It is used here only as the entrainment criterion in the hourly transport formula. If $u_{*j,t}$ does not exceed u_{*t}, hourly potential transport is zero; if the threshold is exceeded, $Q_{j,t}$ is calculated with a Lettau–Lettau-type bulk-flux formula (Ren et al. 2024):

$$Q_{j,t} = 6.7\sqrt{\frac{d}{d_r}}\frac{\rho_a}{g}u_{*,j,t}^3\left(1-\frac{u_{*_t}}{u_{*,j,t}}\right)\Delta t_s, \qquad u_{*,j,t} > u_{*_t} \tag{3}$$

where $d = 0.21$ mm is the site median grain size, $d_r = 0.25$ mm is the reference grain size, $\rho_a = 1.225$ kg m^{-3} is the standard reference air density, $g = 9.81$ m s^{-2} is gravitational acceleration, and $\Delta t_s = 3600$ s is the hourly duration. $Q_{j,t}$ is expressed in kg m^{-1} and represents potential sand mass passing a unit-width section during that hour.

3.6 Deterministic sand transport characterization

The deterministic branch mapped annual potential transport under a common reference entrainment threshold. The site median grain size was $d_{50} = 0.21$ mm, and $u_{*t,50} = 0.265$ m s^{-1} was used as the fixed threshold following the conditional threshold statistics reported by Raffaele et al. (2016). Using $u_{*t,50}$ as the entrainment criterion, hourly $Q_{j,t}$ values were first calculated at the 30 m grid scale using Eq. (3). For grid point j, annual FP was then defined as the scalar accumulation of hourly potential transport converted to volume by the bulk density of deposited sand (ρ_b),

$$\mathrm{FP}_j = \frac{1}{\rho_b}\sum_{t=1}^{N} Q_{j,t} \tag{4}$$

where N is the number of valid hours in a year, ρ_b = 1529 kg m^{-3} is the bulk density of deposited sand, and FP is expressed in m^3 m^{-1} yr^{-1}.

FP measures cumulative potential transport capacity without considering directional cancellation. To characterize the vector resultant effect among transport directions, resultant flux potential (RFP) was calculated from hourly potential transport and transport-to direction. RFP reflects the net transport tendency over the selected time scale and is defined as

$$\mathrm{RFP}_j = \frac{1}{\rho_\mathrm{b}} \sqrt{\left(\sum_{t=1}^{N} Q_{j,t} \sin\theta_{j,t} \right)^2 + \left(\sum_{t=1}^{N} Q_{j,t} \cos\theta_{j,t} \right)^2} \tag{5}$$

The resultant flux direction (RFD) was obtained from the angle of the same vector sum and represents the dominant net transport direction. Directional concentration was summarized by the flux direction variability (FDV), defined as RFP/FP,

$$\mathrm{FDV}_j = \frac{\mathrm{RFP}_j}{\mathrm{FP}_j} \tag{6}$$

FDV ranges from 0 to 1. Values close to 1 indicate a concentrated resultant direction and weak cancellation among transport directions. Deterministic FP, RFP, RFD, and FDV were calculated for each 30 m cell and then area-aggregated to dune patches and engineering units.

3.7 Stochastic sand transport quantification

The stochastic sand-wind probability (SWP) analysis accounted for variability in both the wind and sand fields. The sand component was represented by the probability distribution of threshold friction velocity conditioned on the measured median grain size, using the established relationship between grain diameter and entrainment threshold reported by Raffaele et al. (2016). For the present site, the conditioning diameter was set to the measured median grain size of 0.21 mm. The resulting site-conditioned threshold distribution was parameterized as a Gamma model with coefficient of variation C_v = 0.24 and mean μ_t = 0.265 m s^{-1}, giving shape $k = 1/C_v^2$ and scale $\beta = \mu_t/k$. An independent threshold was drawn for each sampled hour. The cumulative distribution function (F_T) was expressed as

$$u_{*t} \sim F_T, \qquad F_T = \mathrm{Gamma}(k, \beta) \tag{7}$$

The threshold condition in Eq. (3) makes hourly $Q_{j,t}$ a mixed random variable, whereas positive continuous values occur when $u_{*j,t} > u_{*t}$. Since annual FP and vector indices are the sum of these threshold, direction-dependent hourly-scale transports, their distributions cannot be represented in a simple closed-form. Therefore, this paper adopts the stochastic drift potential framework of the Monte Carlo propagation method.

For the wind component, no additional parametric distribution was imposed. Instead, the 2021–2023 archive was treated as an empirical sample of synchronized terrain-downscaled hourly wind fields over the entire domain. For grid cell j, the corresponding marginal empirical distribution of friction velocity and transport direction was expressed as

$$\hat{F}_{W,j} = \frac{1}{T}\sum_{t=1}^{T}\delta_{(u_{*j,t},\theta_{j,t})} \quad (8)$$

where $T = 26280$ is the total number of multi-year hourly samples, and δ is the Dirac measure located at the sample ($u_{*j,t}$, $\theta_{j,t}$). This empirical representation preserves the observed pairing between wind magnitude and transport direction, including short-duration strong-wind conditions that can contribute disproportionately to aeolian transport. Eq. (8) describes the marginal distribution at an individual grid cell, spatial dependence was retained during Monte Carlo resampling by applying a common sampled-hour index to all grid cells, as described below.

In the r-th Monte Carlo realization, a single sequence of N_y hourly indices was drawn with replacement from the common historical index set $\{1, \ldots, T\}$ to form a stochastic representative year, where $N_y = 8760$. The same sequence of sampled indices was applied synchronously to every grid cell j, so that all grid cells at a given sampled position were taken from the same historical hour. The corresponding hourly thresholds were independently sampled from the threshold distribution F_T. The sampling assumes that threshold uncertainty and wind-field variability are independent: the threshold distribution is controlled by grain and bed conditions, whereas hourly friction velocity and transport direction are obtained from the historical downscaled wind fields. For each sampled hour n, the sampled friction velocity and threshold were converted to potential transport $Q_{j,n}(r)$ using the hourly calculation method described in Section 3.5.

Aggregating the N_y hourly values of $Q_{j,n}(r)$ yielded one set of annual aeolian activity indicators, $FP_j(r)$, $RFP_j(r)$, $RFD_j(r)$, and $FDV_j(r)$, for the r-th stochastic representative year. After the random sampling and indicator calculation were repeated M times, with $M = 5000$ in this study, each grid cell had M annual indicator samples. For any indicator Y at grid cell j, these samples define the empirical distribution $\hat{F}_{Y,j}(y)$. The mean, coefficient of variation, and percentiles were then used to describe the typical activity level, dispersion, and uncertainty range. This probabilistic assessment quantifies entrainment-threshold and representative-year wind uncertainty while retaining both the contemporaneous spatial coherence and terrain-induced heterogeneity of the downscaled wind fields.

4 Results

4.1 Dune morphology and terrain characteristics

The original 30 m DEM contains both the broad regional elevation gradient and local dune-scale relief. To isolate the local component, the DEM was smoothed with a Gaussian filter with a standard deviation of 2 pixels, and a background terrain surface was derived with a broader Gaussian filter with a standard deviation of 18 pixels. Relief (m) was calculated as the difference between the smoothed DEM and this background surface. Positive Relief values indicate local terrain higher than the surrounding background and mainly correspond to dune bodies and crest ridges. Negative values indicate local depressions such as interdune areas, and values close to 0 m generally delineate dune margins.

Fig. 5(a) shows the spatial distribution of Relief across the project area. The northwestern part is dominated by values close to 0 m and weak alternation between positive and negative Relief. In contrast, the southern and eastern parts contain dense alternating bands of positive and negative Relief associated with continuous dune relief. High

positive-Relief zones are commonly elongated and ridge-like, corresponding to dune crests, and the positive-negative Relief pattern is especially dense in the southern part of the site.

Dune boundaries were delineated by combining the 65th percentile of Relief with the 55th percentile of local elevation-change intensity calculated using the Sobel operator. Local elevation peaks in the smoothed DEM served as markers for watershed segmentation of connected dune areas. This procedure identified 310 dune patches covering 354.9 km^2, or 40.1% of the 885.2 km^2 effective terrain-analysis area (Fig. 5b). Dunes are concentrated in the central, southern, and eastern sectors, while much of the northwestern sector is classified as non-dune surface.

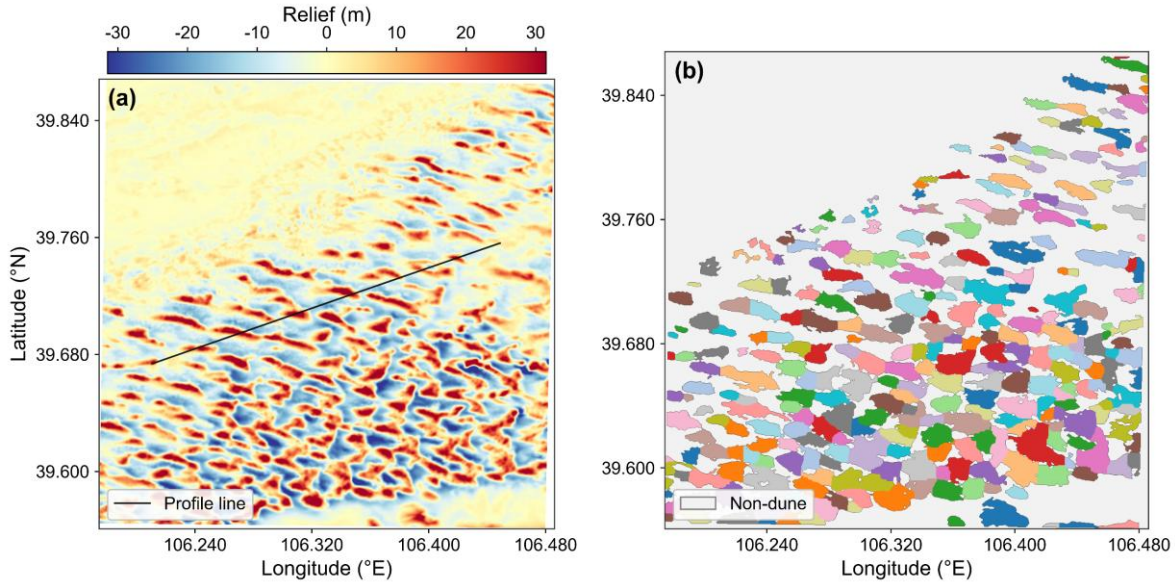


Fig. 5 Dune-scale terrain decomposition and segmentation: (a) local relief; (b) segmented dune patches.

For each dune patch, principal component analysis of centered pixel coordinates defined the major and minor axes. Dune length and width were the maximum projection spans along these axes, area was calculated from the projected 30 m grid-cell area, and height was the within-patch elevation range. The identified dunes vary substantially in planform scale and vertical relief (Fig. 6). Length ranges from 0.45 to 4.00 km, width from 0.20 to 2.40 km, area from 0.12 to 4.33 km^2, and height from 9.8 to 150.2 m (median 70.5 m). Length and width are positively associated (Spearman $\rho = 0.751$), as are area and height ($\rho = 0.764$). 80% of patches have length-to-width ratios between 1 and 2.

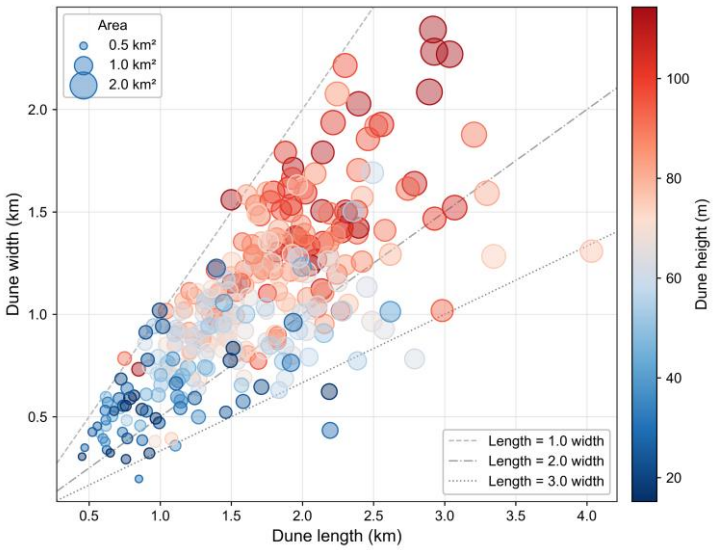


Fig. 6 Planform and vertical morphometry of the 310 identified dune patches, including length, width, area, height, and length-to-width relationships.

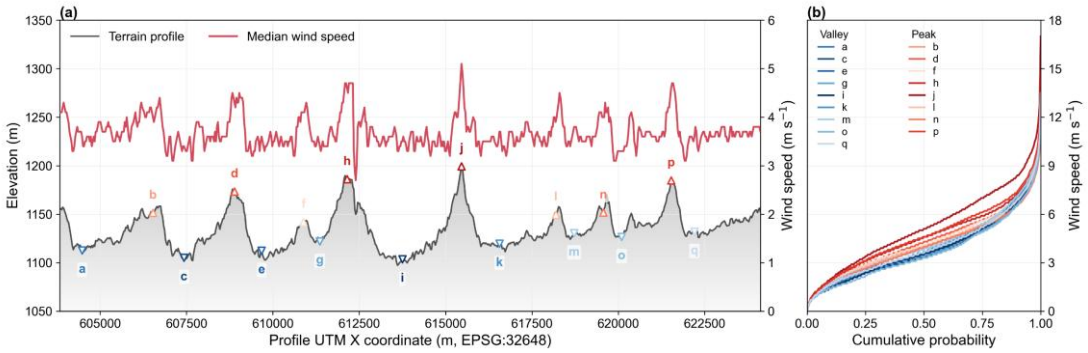
4.2 Topographic effects on the project-site wind field

To illustrate the downscaled wind field under a direction close to the prevailing incoming wind direction of 245°, a representative strong-wind hour was selected. At 12:00 on 7 December 2023, the regional ERA5 10 m wind speed was 11.62 m s^{-1} from 249.35°. The WindNinja wind speed at each grid cell was normalized by the simultaneous ERA5 input speed to obtain the nondimensional wind-speed field shown in Fig. S3.

The downscaled field shows acceleration over dune crests and upper slopes and deceleration in interdune and sheltered areas. The domain-average speed ratio is 0.994, indicating that the COM model mainly redistributes the regional wind forcing. The strongest spatial contrasts occur in the more undulating central and southeastern dune groups, whereas gentler terrain remains closer to the regional input.

To evaluate the long-term influence of dune topography on the downscaled wind field, a 22.4 km profile was extracted along the prevailing incoming wind direction of 245°, with the profile location marked in Fig. 5(a). Fig. 7(a) compares the terrain profile with the median downscaled wind speed calculated from the 2021-2023 hourly samples at sampling points. Median wind speed fluctuated with dune crests and troughs, ranging from 2.7 to 5.1 m s^{-1}. 8 crests and 9 valleys were identified from the smoothed terrain profile, and the highest crest point had a median wind speed of 5.1 m s^{-1}, compared with 3.5 and 3.7 m s^{-1} in the two adjacent valleys. Elevation and median wind speed were significantly correlated along the full profile.

Fig. 7(b) compares the empirical cumulative distributions of hourly wind speed at crest and valley points. Overall, the crest distributions shift toward higher wind speeds relative to the valley distributions. Higher-elevation crests are generally more strongly shifted, whereas the valley curves largely overlap. Crest-valley differences remain visible under moderate to high wind conditions, with mean crest and valley speeds of 5.78 and 5.14 m s^{-1} at the 75th percentile. The relative contrast decreases under the strongest winds, with corresponding values of 8.18 and 7.86 m s^{-1} at the 95th percentile.

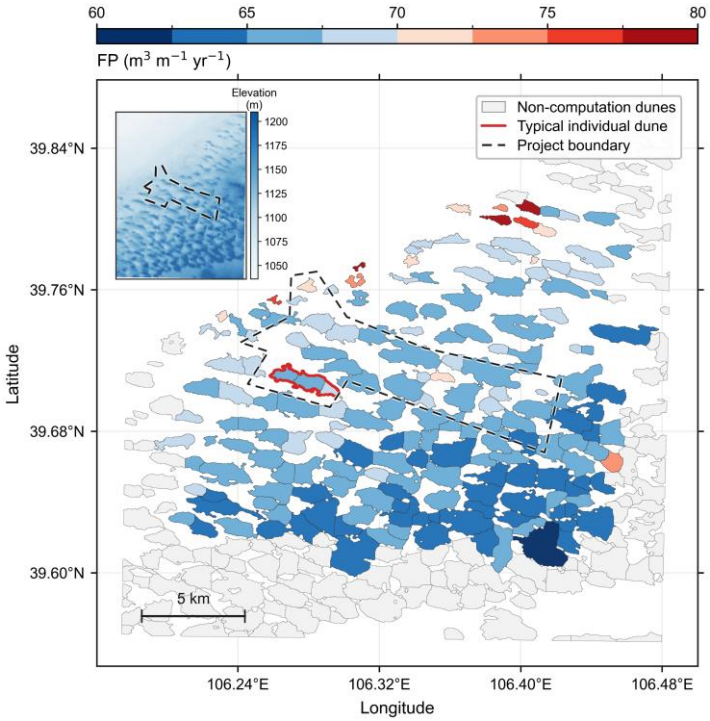


317

318 **Fig. 7** Multi-year terrain-wind response along the 245° prevailing incoming-wind profile: (a) elevation and median 10 m
319 wind speed; (b) empirical hourly wind-speed distributions at crests and valleys.

320 **4.3 Deterministic assessment of potential sand transport**

321 Under the common reference threshold $u_{*t,\mathrm{ref}}$ = 0.265 m s^{-1}, annual mean FP was computed at 30 m and area-
322 averaged within valid dune patches (Fig. 8). These values compare relative potential transport under a common bed
323 condition. Dune identification was performed over a broader terrain-analysis domain, whereas wind downscaling
324 and sand-flux calculations were restricted to the 0.25° × 0.25° core computational domain. As a result, 181 of the
325 310 identified dune patches were included in the Fig. 8 statistics. Their annual FP ranges from 62.08 to 78.22 m^3 m^{-1} yr^{-1}. Higher dune-scale FP values are concentrated mainly in the northwestern part of the core domain, where the
327 terrain is more open and low-relief and therefore less able to block the regional background wind. Many central and
328 southeastern dunes show lower or moderate FP, consistent with denser crest-depression sequences that increase
329 sheltering, repeated uplift, and local deceleration.



330

331 **Fig. 8** Spatial distribution of annual mean FP for individual dunes under the fixed reference threshold.

The representative dune outlined in red in Fig. 8 was selected for internal analysis because it lies inside the project boundary, consists of three connected dune bodies with continuous relief, and is difficult to avoid completely under alternative layout schemes. Within the representative dune, Fig. 9(a) shows strong pixel-scale heterogeneity in annual mean FP. The spatial mean annual FP is 66.0 $m^3\ m^{-1}\ yr^{-1}$, but the local maximum reaches 198.8 $m^3\ m^{-1}\ yr^{-1}$, about 3 times the dune mean. After FP values were ranked from high to low and a 200 m minimum spacing was applied, five separated hotspots were identified. These hotspots occur mainly near crest lines on the northwestern margin, central part, and southeastern margin of the dune.

Fig. 9(b) presents annual mean RFP and resultant transport direction. The mean RFP is 28.9 $m^3\ m^{-1}\ yr^{-1}$, accounting for 43.9% of the mean FP. The RFP-weighted mean transport direction is 87.4°, indicating a predominantly west–east resultant transport pattern, with only small local deviations from east-northeast to east-southeast. Spatially, higher RFP mainly occurs at both ends of the crest line and broadly follows the high-FP zones. Fig. 9(c) maps FDV, which characterizes the directional concentration of sand transport. The dune-mean FDV is 0.441, indicating moderate directional stability and consistent with the RFP-to-FP ratio. Unlike FP and RFP, FDV shows a different spatial pattern, with crest zones generally exhibiting lower values despite their high transport intensity. This indicates that strong transport areas may experience greater directional variability under changing wind conditions. Along the prevailing wind direction, the windward southern slope shows slightly lower FDV than the leeward northern slope, whereas lower leeward areas maintain more stable transport directions.

Within the representative dune, normalized height was calculated for each of the valid grid cells as its elevation relative to the local minimum, scaled by the within-dune elevation range. Grid cells were separated into windward south-facing and leeward north-facing slope groups, and FP, RFP, and FDV were summarized by normalized-height intervals using the median and interquartile range (Fig. S4). Slope-normalized summaries confirm that FP and RFP rise sharply above normalized height 0.7, while FDV decreases toward the crest.

Fig. 9(d) shows monthly cumulative FP at the A-H points, linking internal spatial differences in the representative dune to temporal variability. Points A-D are located on the windward slope, where terrain height increases along the 245° profile, whereas points E-H are located on the leeward slope, where terrain height decreases. The monthly FP curves show similar temporal fluctuations among these points, but their magnitudes differ markedly with slope position. Mean monthly FP is highest at point D on the upper windward slope and lowest at point H on the lower leeward slope, with values of 10.12 and 4.23 $m^3\ m^{-1}\ month^{-1}$, respectively. The other points fall between these two end members. Point D has the highest FP but an FDV of only 0.373, again showing that high transport intensity does not imply a stable resultant direction.

The temporal curves in Fig. 9(d) also show that slope-position contrasts persist through time and are amplified during high-transport months. Across the A-H points, April and May have the highest mean monthly FP, 10.52 and 10.57 $m^3\ m^{-1}\ month^{-1}$, whereas October decreases to 2.15 $m^3\ m^{-1}\ month^{-1}$. The quarterly bars show that Q2 is the only quarter type exceeding 20 $m^3\ m^{-1}\ quarter^{-1}$ in all three years, with values of 26.45, 23.76, and 28.51 $m^3\ m^{-1}\ quarter^{-1}$ for 2021, 2022, and 2023, respectively. By contrast, Q3 and Q4 are lower, while Q1 varies more strongly between years.

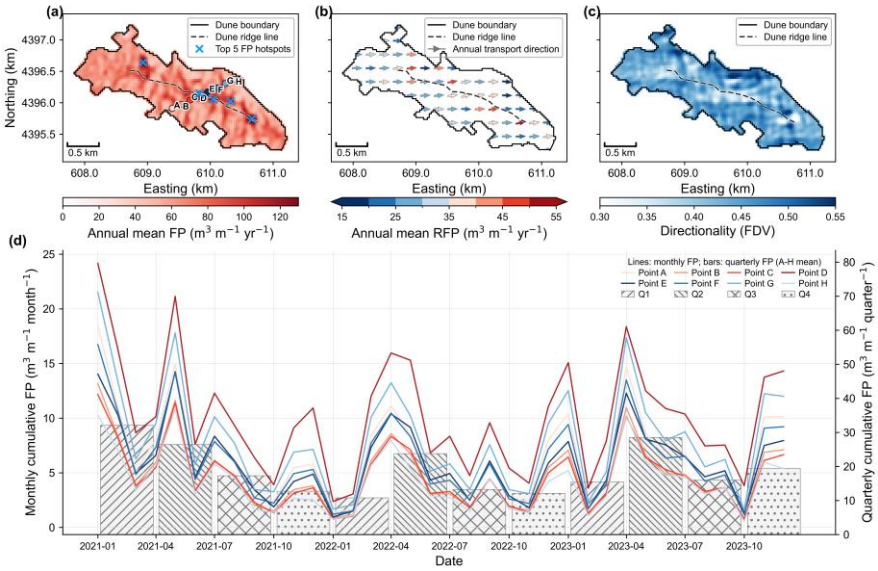
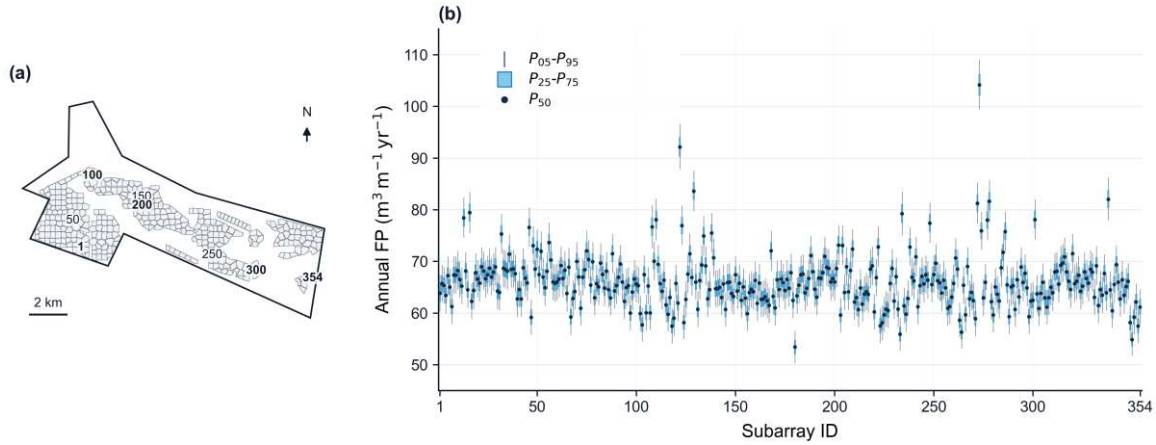


Fig. 9 Deterministic potential transport within the representative dune: (a) annual FP and separated high-value points; (b) annual RFP and resultant transport direction; (c) FDV = RFP/FP; (d) monthly and quarterly FP at profile points A–H.

4.4 Probabilistic quantification of sand drift potential

To quantify annual FP while accounting for stochasticity in both wind speed and threshold friction velocity, the Monte Carlo analysis extends FP from a single deterministic estimate to an empirical probability distribution and aggregates the results over PV subarrays. Here, a subarray denotes an engineering layout unit in the preliminary PV-plant design, composed of strip-like module rows. A standard subarray contains 20 rows with a 10.23 m clear spacing and spans about 270 m in both east-west and north-south directions, while non-standard subarrays are used where terrain or boundaries are irregular. The subarray outlines were extracted from the design CAD files, transformed to WGS84, and clipped to the actual project boundary, yielding 354 subarrays (Fig. 10a).

Based on these spatial units, Fig. 10(b) summarizes annual FP distributions from 5000 stochastic representative-year simulations. The horizontal axis retains the natural engineering-unit order from Subarray ID 1 to 354. For each subarray, P_{05}, P_{25}, P_{50}, P_{75}, and P_{95} were calculated. The vertical P_{05}-P_{95} interval represents the broader uncertainty range, the P_{25}-P_{75} box represents the main concentration interval, and the dark point represents P_{50}. Most subarray P_{50} values cluster around 60-70 $m^3\ m^{-1}\ yr^{-1}$, with a small number of high-value peaks. Individual P_{05}-P_{95} widths range from 6.27 to 9.63 $m^3\ m^{-1}\ yr^{-1}$, much smaller than the spatial range of subarray P_{50} values. Monte Carlo variability therefore broadens estimates around each subarray's typical FP level without masking the relative contrasts caused by spatial heterogeneity. Across all 1.77 million subarray-realization values, pooled P_{50} is 65.63 $m^3\ m^{-1}\ yr^{-1}$ and pooled P_{05}-P_{95} is 58.46-75.74 $m^3\ m^{-1}\ yr^{-1}$.

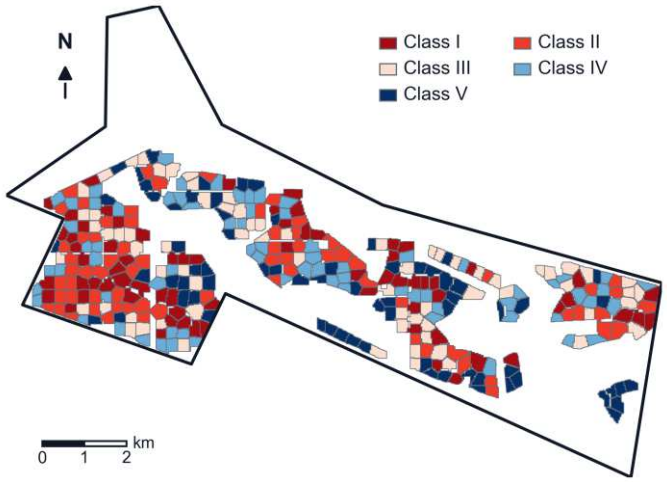


388

389 **Fig. 10** PV subarray distribution and probabilistic annual FP results: (a) spatial distribution of the 354 PV subarrays; (b)
390 compact natural-order quantile glyphs. Vertical intervals denote P_{05}-P_{95}, boxes denote P_{25}-P_{75}, and points denote P_{50}.

391 Building on Fig. 10, the subarrays were classified by stochastic relative activity. In each Monte Carlo realization,
392 all 354 subarrays were ranked from high to low annual FP and divided into five nearly equal-capacity intervals.
393 Each subarray therefore received 5000 class records, and its final class was assigned by the most frequent class; ties
394 were resolved using the mean rank across all simulations.

395 Fig. 11 maps the resulting activity classes. Classes I, II, III, IV, and V contain 71, 70, 71, 72, and 70 subarrays,
396 respectively. The current layout already avoids much of the highly active northwestern dune zone, but Classes I and
397 II still concentrate near crest lines of representative northwestern dunes, whereas Classes IV and V occur more often
398 along central-eastern dune-foot margins. Detailed class-specific annual FP density structures for Classes I, III, and
399 V are provided in Supplementary Fig. S5.



400

401 **Fig. 11** Stochastic-ranking activity classes for 354 PV subarrays. Colors denote the five relative within-site priority classes
402 (I-V) assigned from 5000 Monte Carlo representative-year realizations.

403 To convert the stochastic-ranking classes into directly comparable aeolian-activity magnitudes, Table 1 pools the
404 5000 annual FP samples of all subarrays within each class and extracts P_{05}, P_{25}, P_{50}, P_{75}, and P_{95} from each class-

level distribution. RIW is calculated as (P_{95} - P_{05})/P_{50} to describe the relative spread of annual FP. The table also reports the RFP-weighted RFD, a circular mean resultant direction weighted by deterministic RFP, and the median FDV for each class.

Table 1 Class-wise probabilistic and directional summary of annual FP for the five activity classes.

Class	FP (m^3 m^{-1} yr^{-1})					RIW	RFP-weighted RFD (deg)	Median FDV
	P_{05}	P_{25}	P_{50}	P_{75}	P_{95}			
I	66.54	69.36	71.88	75.72	83.24	0.23	84.61	0.411
II	63.76	65.95	67.52	69.14	71.40	0.11	86.31	0.416
III	62.03	64.15	65.65	67.21	69.38	0.11	86.88	0.416
IV	60.09	62.22	63.74	65.30	67.48	0.12	87.25	0.420
V	55.40	58.49	60.40	62.19	64.65	0.15	88.11	0.425

The class statistics show a clear FP intensity gradient. Pooled P_{50} decreases from 71.88 m^3 m^{-1} yr^{-1} in Class I to 60.40 m^3 m^{-1} yr^{-1} in Class V. The Class I P_{05} (66.54 m^3 m^{-1} yr^{-1}) still exceeds the Class V P_{95} (64.65 m^3 m^{-1} yr^{-1}), indicating a distinct separation between the highest and lowest activity classes. Class I has the largest RIW (0.23), showing that high-activity subarrays combine stronger typical transport potential with a broader high-percentile response. Classes II-IV are more compact (RIW = 0.11-0.12), while Class V retains a visible spread (RIW = 0.15). Directional contrast was weaker, with the RFP-weighted RFD ranging from 84.61° to 88.11°, while median FDV increased only slightly from 0.411 in Class I to 0.425 in Class V. Considering annual FP, RIW, and ranking stability together, Classes I and II should be prioritized for sand-control design, inspection, maintenance, and local reinforcement. Class III is a transitional management zone, whereas Classes IV and V are more suitable for routine maintenance and adaptive adjustment.

5 Discussion

This study addresses a scale of aeolian assessment between regional desert-PV site suitability and local near-field sand transport around PV arrays. Regional studies can identify deserts with high or low sand-flux potential using coarse reanalysis winds, as in the global desert solar-farm assessment of Li et al. (2024). Array-scale experiments, by contrast, can reveal how PV modules modify near-surface transport and erosion-deposition patterns, as shown by Tang et al. (2021). The present framework targets the intermediate engineering scale inside an already selected PV site, where dune morphology, slope position, and subarray layout control the spatial priority of windblown-sand management.

The methodological contribution is an independently evaluated link between regional hourly forcing and site-internal management units. The Askervein benchmark shows that the COM solver reproduces terrain-scale wind-speed variation without fitting to the validation points; r = 0.949 across 40 observations. This performance is consistent with the recognized importance of terrain correction in spatial meteorological modelling (Liston and Elder 2006) and with recent engineering applications of terrain- and roughness-adjusted reanalysis winds (Yang et al. 2022; Raffaele et al. 2024). At the project site, COM redistributes the 2021-2023 ERA5 wind series over 30 m dune terrain, while FP and RFP translate the downscaled winds into aeolian activity metrics. Coupling these metrics with

threshold friction velocity uncertainty and Monte Carlo representative-year sampling extends the analysis from deterministic mapping to probability distributions and ranking stability for PV subarrays.

The terrain-control patterns obtained here are consistent with recent dune-flow and dune-migration studies and extend them to a continuous-dune PV setting. Daudon et al. (2024) showed that including topographic speed-up can increase predicted sand flux and barchan migration rates by approximately a factor of three, and Louge et al. (2024) demonstrated that shear velocity over large barchans is not a simple monotonic function of elevation because roughness transitions and dune shape create local anomalies near crests and brinks. In the present site, the representative dune has a local FP maximum of 198.8 $m^3\ m^{-1}\ yr^{-1}$, approximately 3 times its mean (66.0 $m^3\ m^{-1}\ yr^{-1}$), and the upper windward point has about 2.4 times the annual FP of the lower leeward point. At the same time, normalized height is positively correlated with FP and RFP but negatively correlated with FDV. These results indicate that terrain speed-up primarily amplifies transport intensity, whereas directionality remains controlled by vector cancellation under variable winds and slope-dependent flow redistribution.

The temporal and probabilistic results show why hourly forcing and uncertainty propagation are needed for this type of assessment. Reanalysis winds entering dune fields can acquire local expressions that depend on relief, boundary-layer conditions, and wind-speed class (Gadal et al. 2022). Strong wind events can also dominate cumulative dune movement despite occupying a small fraction of the record because sand flux responds nonlinearly once the threshold is exceeded (Ren et al. 2024). The deterministic results from the representative dune show this time concentration through the dominance of late spring and early summer FP. The Monte Carlo results show that uncertainty in threshold friction velocity and representative year sampling broadens annual FP distributions without removing the spatial separation between high- and low-activity classes. This finding is consistent with probabilistic windblown-sand action concepts, which emphasize characteristic values and maintenance relevance rather than mean transport alone (Raffaele et al. 2016).

Several limitations define the application boundary of the present framework. FP, RFP, RFD, and FDV represent potential or saturated sand-transport capacity under ERA5 forcing, COM terrain redistribution, and specified threshold conditions. They do not explicitly account for sand-supply limitation or surface moisture, both of which can affect actual erosion and deposition. The COM model is also designed to represent relative terrain-induced speed-up and direction adjustment at low computational cost; it does not resolve separation or turbulent structures around components. Future work should combine field sensors, repeated UAV topographic surveys, and CFD or wind-tunnel tests for key subarrays to calibrate potential FP against observed erosion-deposition patterns and maintenance thresholds.

6 Conclusions

This study developed an hourly probabilistic framework for site-internal sand-drift assessment in a desert PV project by integrating 2021–2023 ERA5 winds, a 30 m DEM, COM terrain downscaling, deterministic transport indicators, and Monte Carlo uncertainty propagation. The COM downscaling method was independently validated against field observations and showed good agreement, with a Pearson correlation coefficient of 0.949. The framework translates regional forcing into FP, RFP, RFD, and FDV at grid, dune, and subarray scales, thereby resolving spatial

heterogeneity, annual FP uncertainty, and stochastic subarray ranking.

Terrain downscaling consistently produced acceleration over dune crests and upper slopes and deceleration in interdune and sheltered terrain. Dunes in more exposed surroundings exhibited higher overall FP, while local hotspots were concentrated near crests and upper windward slopes, where FP reached approximately three times the dune mean. Directional characteristics followed a different spatial pattern, with high-transport crest zones generally showing lower FDV and greater directional variability than lower leeward areas. Monte Carlo analysis showed that uncertainty in threshold friction velocity and representative annual winds broadened annual FP distributions without removing terrain-controlled spatial contrasts. The pooled annual FP distribution had a P_{50} of 65.63 $m^3\ m^{-1}\ yr^{-1}$ and a P_{05}–P_{95} range of 58.46–75.74 $m^3\ m^{-1}\ yr^{-1}$. The five stochastic classes remained clearly separated, with pooled P_{50} decreasing from 71.88 $m^3\ m^{-1}\ yr^{-1}$ in Class I to 60.40 $m^3\ m^{-1}\ yr^{-1}$ in Class V, while the Class I P_{05} exceeded the Class V P_{95}. The proposed framework translates regional aeolian forcing into sand-drift zoning within desert PV projects, supporting the identification of high potential dune areas and PV subarrays for layout optimization and targeted sand control.

References

Al-Hemoud, A., Alqahtani, J., Mhawish, A., et al., 2026. Sand and dust storms, sand encroachment, and drought in Kuwait: a basis for formulating a disaster risk reduction plan. Natural Hazards 122, 81.

Bruno, L., Horvat, M., Raffaele, L., 2018. Windblown sand along railway infrastructures: a review of challenges and mitigation measures. Journal of Wind Engineering and Industrial Aerodynamics 177, 340–365.

Daudon, C., Beyers, M., Jackson, D., et al., 2024. Prediction of barchan dunes migration using climatic models and speed-up effect of dune topography on air flow. Earth and Planetary Science Letters 648, 119049.

European Space Agency, 2024. Copernicus Global Digital Elevation Model. Distributed by OpenTopography.

Forthofer, J.M., Butler, B.W., Wagenbrenner, N.S., 2014. A comparison of three approaches for simulating fine-scale surface winds in support of wildland fire management. Part I. Model formulation and comparison against measurements. International Journal of Wildland Fire 23(7), 969–981.

Fryberger, S.G., Dean, G., 1979. Dune forms and wind regime. In: McKee, E.D. (Ed.), A Study of Global Sand Seas. U.S. Geological Survey Professional Paper 1052, Washington, DC, pp. 137–169.

Gadal, C., Delorme, P., Narteau, C., et al., 2022. Local wind regime induced by giant linear dunes: comparison of ERA5-Land reanalysis with surface measurements. Boundary-Layer Meteorology 185, 309–332.

Gageik, M., Rodriguez Ahlert, C.J., Coste, N., et al., 2024. A multi-scale gap-bridging CWE approach to windblown sand action on critical infrastructures: modelling framework and case study on a high-speed railway line. Journal of Wind Engineering and Industrial Aerodynamics 249, 105722.

Gunn, A., Casasanta, G., Di Liberto, L., et al., 2022. What sets aeolian dune height? Nature Communications 13, 2401.

Hersbach, H., Bell, B., Berrisford, P., et al., 2023. ERA5 hourly data on single levels from 1940 to present. Copernicus Climate Change Service Climate Data Store.

Hugenholtz, C.H., Levin, N., Barchyn, T.E., et al., 2012. Remote sensing and spatial analysis of aeolian sand dunes: a review and outlook. Earth-Science Reviews 111(3–4), 319–334.

Kok, J.F., Parteli, E.J.R., Michaels, T.I., et al., 2012. The physics of wind-blown sand and dust. Reports on Progress in Physics 75(10), 106901.

Kruitwagen, L., Story, K.T., Friedrich, J., et al., 2021. A global inventory of photovoltaic solar energy generating units. Nature 598, 604–610.

Li, G., Tan, L., Yang, B., et al., 2024. Site selection of desert solar farms based on heterogeneous sand flux. npj Climate and Atmospheric Science 7, 61.

Liston, G.E., Elder, K., 2006. A meteorological distribution system for high-resolution terrestrial modelling (MicroMet). Journal of Hydrometeorology 7(2), 217–234.

Louge, M.Y., Valance, A., Fang, J., et al., 2024. Evolution of turbulent boundary conditions on the surface of large barchan dunes: anomalies in aerodynamic roughness and shear velocity, aeolian threshold, and the role of dune skewness. Journal of Geophysical Research: Earth Surface 129(9), e2023JF007599.

Lu, Z., Zhang, Q., Miller, P.A., et al., 2021. Impacts of large-scale Sahara solar farms on global climate and vegetation cover. Geophysical Research Letters 48(2), e2020GL090789.

Muñoz-Sabater, J., Dutra, E., Agustí-Panareda, A., et al., 2021. ERA5-Land: a state-of-the-art global reanalysis dataset for land applications. Earth System Science Data 13(9), 4349–4383.

Powers, J.G., Klemp, J.B., Skamarock, W.C., et al., 2017. The Weather Research and Forecasting Model: overview, system efforts, and future directions. Bulletin of the American Meteorological Society 98(8), 1717–1737.

Raffaele, L., Bruno, L., Pellerey, F., et al., 2016. Windblown sand saltation: a statistical approach to fluid threshold shear velocity. Aeolian Research 23, 79–91.

Raffaele, L., Bruno, L., Colucci, E., 2024. Reanalysis-based mesoscale wind maps for the design of structures and infrastructures with an application to Italy. Journal of Wind Engineering and Industrial Aerodynamics 253, 105844.

Ren, H., Gao, X., Zhao, Y., et al., 2024. Strong-wind events control barchan dune migration. Communications Earth & Environment 5, 278.

Tadesse, A., Jeong, J., Green, C.H.M., 2022. Modeling landscape wind erosion processes on rangelands using the APEX model. Ecological Modelling 467, 109925.

Tang, G., Meng, Z., Gao, Y., et al., 2021. Impact of utility-scale solar photovoltaic array on the aeolian sediment transport in Hobq Desert, China. Journal of Arid Land 13(3), 274–289.

Taylor, P.A., Teunissen, H.W., 1987. The Askervein Hill project: overview and background data. Boundary-Layer Meteorology 39(1), 15–39. https://doi.org/10.1007/BF00121863

Wagenbrenner, N.S., Forthofer, J.M., Lamb, B.K., et al., 2016. Downscaling surface wind predictions from numerical weather prediction models in complex terrain with WindNinja. Atmospheric Chemistry and Physics 16(8), 5229–5241.

Wagenbrenner, N.S., Forthofer, J.M., Page, W.G., et al., 2019. Development and evaluation of a Reynolds-averaged Navier–Stokes solver in WindNinja for operational wildland fire applications. Atmosphere 10(11), 672. https://doi.org/10.3390/atmos10110672

Wang, J., Wang, Y., Yan, C., Qi, Y., 2013. 1:100,000 desert (sand) distribution dataset in China. National Tibetan Plateau/Third Pole Environment Data Center.

Wiggs, G.F.S., Livingstone, I., Warren, A., 1996. The role of streamline curvature in sand dune dynamics: evidence from field and wind tunnel measurements. Geomorphology 17(1–3), 29–46.

Yang, S., Chouinard, L.E., Langlois, S., 2022. Hourly wind data for aeolian vibration analysis of overhead transmission line conductors. Journal of Wind Engineering and Industrial Aerodynamics 230, 105184.

Yizhaq, H., Xu, Z., Ashkenazy, Y., 2020. The effect of wind speed averaging time on the calculation of sand drift potential: new scaling laws. Earth and Planetary Science Letters 544, 116373.

Statements & Declarations

This work was supported by the National Natural Science Foundation of China [grant number 52278511]. The authors have no relevant financial or non-financial interests to disclose.

Author Contributions

Sai Li: Writing – original draft, Visualization, Methodology, Investigation, Data curation. Wenyong Ma: Writing – review and editing, Validation, Funding acquisition, Conceptualization. Bingbing Wang: Validation, Supervision, Resources. Lingui Xin: Writing – review and editing, Formal analysis. Junxiang Ma: Resources, Project administration.

Supplementary Files

This is a list of supplementary files associated with this preprint. Click to download.

- Supplementarymaterial.docx